AGU PUBLICATIONS

JGR

Journal of Geophysical Research: Solid Earth

RESEARCH ARTICLE
10.1002/2017JB014558

Special Section:
Seismic and micro-seismic signature of fluids in rocks: Bridging the scale gap

Sensitivity of Seismic Attenuation and Phase Velocity to Intrinsic Background Anisotropy in Fractured Porous Rocks: A Numerical Study

Nicolás D. Barbosa[1], **J. Germán Rubino**[2], **Eva Caspari**[1], **and Klaus Holliger**[1]

[1] Applied and Environmental Geophysics Group, Institute of Earth Sciences, University of Lausanne, Lausanne, Switzerland, [2] CONICET, Centro Atómico Bariloche-CNEA, San Carlos de Bariloche, Argentina

Key Points:
- Numerical study of wave-induced fluid flow effects in fractured rocks in the presence of intrinsic background anisotropy
- Hydraulic and elastic intrinsic anisotropy of the background strongly affects the phase velocity and attenuation anisotropy of fractured rocks
- Accounting for the effects of intrinsic background anisotropy is crucial for fracture and hydraulic parameters estimation

Correspondence to:
N. D. Barbosa,
nicolas.barbosa@unil.ch

Citation:
Barbosa, N. D., Rubino, J. G., Caspari, E., & Holliger, K. (2017). Sensitivity of seismic attenuation and phase velocity to intrinsic background anisotropy in fractured porous rocks: A numerical study. *Journal of Geophysical Research: Solid Earth*, *122*, 8181–8199. https://doi.org/10.1002/2017JB014558

Received 13 JUN 2017
Accepted 6 OCT 2017
Accepted article online 9 OCT 2017
Published online 26 OCT 2017

Abstract Many researchers have analyzed seismic attenuation and velocity dispersion due to wave-induced fluid flow (WIFF) related to the presence of fluid-saturated fractures embedded in an isotropic porous background. Most fractured formations do, however, exhibit some degree of intrinsic elastic and hydraulic anisotropy of the background, and the impact of which on the effective seismic properties remains largely unexplored. In this work, we extend a numerical upscaling procedure to account for the potential intrinsic elastic and hydraulic anisotropy of the background. To do this, we represent the background of a representative sample of the fractured formation of interest with an anisotropic poroelastic medium and apply a set of relaxation experiments to compute the effective anisotropic seismic properties. A comprehensive numerical analysis allows us to observe that, for samples containing hydraulically connected fractures, the anisotropic behavior of both *P* and *S* waves differs significantly from that observed for an isotropic background. The anisotropy of the stiffness of the background plays a fundamental role for WIFF between the fractures and the background as well as for WIFF between connected fractures. Conversely, the anisotropy of the background permeability affects the characteristic frequency, the angle dependence, and the magnitude of the effects related to WIFF between fractures and background. In addition, different correlations between hydraulic and elastic background anisotropy lead to different degrees of effective seismic anisotropy. Our results therefore indicate that accounting for the effects of intrinsic background anisotropy on WIFF is crucial for a quantitative interpretation of seismic anisotropy measurements in fluid-saturated fractured formations.

1. Introduction

Seismic methods are widely considered a valuable tool for effectively characterizing fluid-saturated heterogeneous porous rocks. One of the reasons for this is that when a seismic wave propagates through fluid-saturated formations containing heterogeneities in the mesoscopic scale range, that is, at scales smaller than the prevailing wavelengths but larger than the typical grain size, it experiences significant attenuation and phase velocity dispersion due to a mechanism broadly known as wave-induced fluid flow (WIFF) (e.g., Müller et al., 2010; Pride, 2005). As fractures tend to dominate the reservoirs' mechanical and hydraulic properties, there is great interest in improving the seismic characterization of fractured environments for a wide range of applications throughout the Earth, environmental, and engineering sciences (e.g., Laubach et al., 2000; Liu & Martinez 2013, Zhang et al., 2009). Since, in most cases, the resolution of seismic data is too low for directly imaging fractures, most of the related research efforts focus on understanding the link between seismic anisotropy attributes, such as shear wave splitting and azimuthal variations in *P* wave attenuation and phase velocity, and fracture characteristics (e.g., Bakulin et al., 2000; Maultzsch et al., 2007). However, in most environments, the observed anisotropy is not only related to the presence of fractures but also due to the intrinsic anisotropy of the host rocks (e.g., Tsvankin, 1997). In this kind of scenario, the adequacy of fracture characterization relies on the ability to account for both effects.

There has been a significant progress in recent decades toward the understanding of how the physical, geometrical, and hydraulic properties of fractured rocks affect WIFF and, correspondingly, the effective anisotropic seismic response. It is well known that at the mesoscale, WIFF occurs between fractures and the pore space of the embedding background (FB-WIFF) (e.g., Brajanovski et al., 2005; Chapman, 2003) as well as within hydraulically connected permeable fractures (FF-WIFF) (e.g., Rubino et al., 2013; Quintal et al., 2014;

Vinci et al., 2014). The magnitude of the FB-WIFF and FF-WIFF effects is related to the fluid pressure gradients established between the fractures and the surrounding background and between hydraulically connected fractures, respectively, in response to the passing seismic wave. This implies that any seismic signature of the corresponding fluid pressure equilibration process involved may contain information of the properties of the fracture network (orientation, compliance, geometrical characteristics, permeability, etc.), saturating fluid (viscosity, bulk modulus, and saturation), and background rock (stiffness, permeability, intrinsic anisotropy, etc.) (Guo et al., 2016).

The theoretical model developed by Chapman (2003) is likely to be the most extensively used approach for fracture parameter inversion using frequency-dependent seismic anisotropy (e.g., Maultzsch et al., 2003; Tillotson et al., 2014). The model assumes two crack populations consisting of randomly aligned ellipsoidal microcracks at the grain scale and aligned ellipsoidal fractures at the mesoscale. The frequency-dependent seismic anisotropy in fractured porous rocks is modeled as a function of the host rock porosity and permeability, the fracture density and orientation, and the pore fluid properties. However, the model of Chapman (2003) is limited to dilute concentrations of fractures and does not take into account FF-WIFF. Chapman (2009) extended his original model to account for two sets of mesoscale fractures with different scale lengths and orientations. He included the effects on the relaxation process due to the presence of two characteristic fracture length scales, but the effects due to hydraulically connected fractures remain unaccounted for.

Conversely, the numerical methodology employed by Rubino et al. (2013, 2014) allows to account for both FB-WIFF and FF-WIFF effects as well as fracture interaction effects commonly associated with higher fracture densities. For the case of fractured rocks containing hydraulically connected fractures, Rubino et al. (2014) performed an exhaustive sensitivity analysis of FF-WIFF effects on *P* wave propagation for different fracture and background properties. Vinci et al. (2014) corroborated these findings on FF-WIFF effects on *P* wave propagation by using a hybrid-dimensional approach in which FF-WIFF was modeled as a one-dimensional process. Quintal et al. (2014) performed a corresponding sensitivity analysis for *S* waves. Recently, Guo et al. (2016) developed a theoretical framework based on the linear slip theory to quantify the FB-WIFF and FF-WIFF effects on the frequency-dependent elastic properties of saturated isotropic porous rocks containing two sets of intersecting fractures. They observed very good agreement between the theoretical predictions and the values obtained from corresponding numerical simulations. Rubino et al. (2016) extended the numerical methodology of Rubino et al. (2013) to compute the seismic properties of a poroelastic sample in the presence of generic effective anisotropy.

The common aspect shared by all these works is that the modeling of the embedding background is limited to an isotropic medium. Most fractured formations are, however, characterized by intrinsic background anisotropy (e.g., Bakulin et al., 2000), which implies that their effective anisotropy is produced by the combined effects of fractures and anisotropic background. Wang (2002) presented measurements of velocity anisotropy in shale and various reservoir rocks showing that the intrinsic anisotropy of tight sands, shaly sands, siltstones, or thin sandshale sequences may exceed 10%. Interestingly, this is also an issue when dealing with manufactured cracked samples (Ding et al., 2017; Tillotson et al., 2014). Tillotson et al. (2014) explained that the manufacturing process of samples containing penny-shaped cracks leads to bedding fabric anisotropy in response to the successive packing of the crack layers composing the sample.

To date, most efforts to include the effects of the elastic intrinsic anisotropy of the background on the seismic response of fractured rocks are based on the linear slip theory (Schoenberg, 1980). That is, the effective compliance matrix of the fractured rock is obtained by simply adding the excess fracture compliance to the compliance of the anisotropic background (Bakulin et al., 2000). Although this approach is reasonable for dry rocks when fracture interactions can be neglected or in the absence of fluid pressure diffusion processes, the impact of intrinsic anisotropy of the background on FB-WIFF and FF-WIFF effects in fractured rocks remains largely unexplored. Recent efforts in this direction include the works of Tillotson et al. (2014) and Ding et al. (2017), who adapted Chapman's (2003) model to account for the intrinsic anisotropy of a laboratory sample in a poroelastic framework. However, in addition to the limitations of Chapman's (2003) model mentioned above, the corrections to the overall stiffness associated with the presence of fractures are still calculated based on an isotropic background medium. Lastly, it has been pointed out that materials possessing intrinsic elastic anisotropy are likely to exhibit anisotropic permeability as well (Carcione, 2007; Gelinsky & Shapiro, 1997; Martin & Brown, 1996). However, to the best of our knowledge, there are no models accounting for

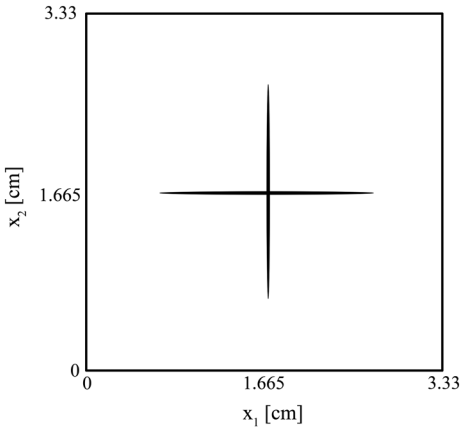

Figure 1. Synthetic sample representing a unit cell of a periodically fractured rock containing two connected orthogonal fractures. The background is assumed to be transversely isotropic with its symmetry axis parallel to the x_2 direction.

the hydraulic intrinsic anisotropy of the background in fractured media to compute its effective anisotropic seismic response.

In this work, we extend the methodology of Rubino et al. (2016) to explore the effective anisotropic behavior of *P* and *S* waves related to the presence of fluid-saturated fractures embedded in a background whose mechanical and hydraulic properties can be intrinsically anisotropic. Biot's (1962) theory provides a convenient framework for the study of intrinsic anisotropy as it allows to represent a medium that is microscopically inhomogeneous with a homogeneous anisotropic poroelastic effective medium. Our methodology consists in the application of a set of numerical oscillatory relaxation tests based on the theory of anisotropic poroelasticity to a 2-D synthetic rock sample representative of a fractured formation of interest. The resulting volume-averaged stress-strain behavior of the sample allows us to compute effective anisotropic seismic attenuation and velocity dispersion. We perform a sensitivity analysis to explore the role played by the intrinsic anisotropy of the background on the FB-WIFF and FF-WIFF regimes of seismic attenuation and phase velocity dispersion.

2. Methodology

For the study of WIFF effects in presence of intrinsic anisotropy of the background, we consider a representative elementary volume of a fractured porous rock (Figure 1) and compute its effective anisotropic response by applying a set of three oscillatory relaxation experiments based on a numerical solution of the quasi-static approximation of Biot's (1962) equations. The reasoning behind this is that, for frequencies much smaller than Biot's critical frequency, the underlying physical process is controlled by fluid pressure diffusion, and thus, inertial effects can be neglected.

In order to extend the methodology of Rubino et al. (2016) to the case of an intrinsically anisotropic background, we represent the background with a homogeneous and anisotropic poroelastic medium. That is, we assume that the intrinsic anisotropy of the background is produced by heterogeneities at the microscopic scale due to, for example, preferential alignment of minerals, fine layering of sedimentary materials of different stiffness, or stress-induced anisotropy (e.g., Dürrast et al., 2002; Wang, 2002). Furthermore, as these heterogeneities can cause not only elastic anisotropy but also hydraulic anisotropy, we allow the background permeability to be anisotropic by considering a permeability tensor (e.g., Dubos-Sallée & Rasolofosaon, 2011). The fractures, on the other hand, are in the mesoscopic scale range and are assumed to be composed of an isotropic and highly compliant poroelastic medium characterized by very high porosity and permeability. Both the fractures and the background are fully fluid saturated.

Following Rubino et al. (2016), we use a set of three oscillatory relaxation tests to infer effective anisotropic properties of the sample of interest. The first test consists of the application of homogeneous time-harmonic normal displacements along the top and bottom boundaries of the sample, while the lateral boundaries are confined (Figure 2a). The second test is similar to the previous one, but the normal displacements are applied on the lateral boundaries of the sample (Figure 2b). Finally, in the third test, we apply a simple shear to the probed sample (Figure 2c). As we are interested in the undrained response, we do not allow the fluid to flow into the sample or out of it in any of the three numerical experiments. The solid and relative fluid displacement fields resulting from each oscillatory relaxation test are obtained by solving the quasi-static poroelastic equations (Biot, 1962) in the space-frequency domain under corresponding boundary conditions

$$\nabla \cdot \boldsymbol{\sigma} = \mathbf{0}, \tag{1}$$

$$i\omega \mathbf{w} = -\frac{\boldsymbol{\kappa}}{\eta} \nabla p_f, \tag{2}$$

where ω is the angular frequency, $\boldsymbol{\sigma}$ is the total stress tensor, p_f the fluid pressure, $\mathbf{w}$ the average relative fluid displacement, and η the shear viscosity of the pore fluid. In order to account for the hydraulic anisotropy in the background, the permeability $\boldsymbol{\kappa}$ is defined as a symmetric second-rank tensor with six independent coefficients (e.g., Biot, 1962; Dubos-Sallée & Rasolofosaon, 2011)

$$\boldsymbol{\kappa} = \begin{bmatrix} \kappa_{11} & \kappa_{12} & \kappa_{13} \\ \kappa_{12} & \kappa_{22} & \kappa_{23} \\ \kappa_{13} & \kappa_{23} & \kappa_{33} \end{bmatrix}. \tag{3}$$

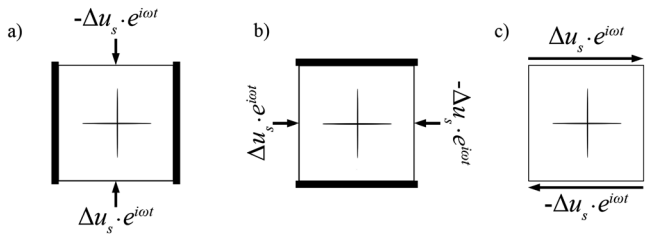

Figure 2. Schematic illustration of the (a) vertical, (b) horizontal, and (c) shear numerical oscillatory relaxation tests employed for determining the components of an equivalent stiffness matrix of fractured rocks.

Due to the anisotropic nature of the mechanical properties of the background, equations (1) and (2) are coupled through the anisotropic poroelastic constitutive relations (Biot, 1962). In the case of 2-D numerical experiments, we assume plane strain conditions to neglect the strain variations along the third dimension, thus ensuring that the effective anisotropic properties obtained are physically meaningful. For the chosen coordinate system (Figure 1), this implies that (i) fractures are long enough in the x_3 direction and (ii) that the x_1-x_2 plane must be a plane of symmetry of the background anisotropy. The latter, in turn, means that, for 2-D numerical experiments, the lowest symmetry possible for the background is monoclinic (Mavko et al., 2009), in which case the x_1-x_2 plane must coincide with the single plane of mirror symmetry of the background. Hence, under plane strain conditions normal to the x_3 axis, the most general background constitutive relations in the x_1-x_2 plane are (Carcione, 2007)

$$\begin{bmatrix} \sigma_{11} \\ \sigma_{22} \\ \sigma_{12} \\ p_f \end{bmatrix} = \begin{bmatrix} C^s_{11} & C^s_{12} & C^s_{16} & -\alpha_1 M \\ C^s_{12} & C^s_{22} & C^s_{26} & -\alpha_2 M \\ C^s_{16} & C^s_{26} & C^s_{66} & 0 \\ -\alpha_1 M & -\alpha_2 M & 0 & M \end{bmatrix} \cdot \begin{bmatrix} \varepsilon_{11} \\ \varepsilon_{22} \\ 2\varepsilon_{12} \\ \zeta \end{bmatrix}, \tag{4}$$

where ε_{ij} is the strain tensor, $\zeta = -\nabla \cdot \mathbf{w}$ is the local change in pore fluid content, α_i are the effective Biot-Willis stress coefficients, M is the analogue of Gassmann's pore space modulus and the stiffness elements C^s_{ij} correspond to the saturated frame. For the medium representing the fractures, equations (3) and (4) reduce to their isotropic forms.

By solving equations (1) and (2) coupled with equation (4), we compute for each numerical test the solid and relative fluid displacement fields from which the stress and strain fields can be obtained. Then, we evaluate the corresponding averages over the sample's volume

$$< \varepsilon^k_{ij} > = \frac{1}{V} \int_\Omega \varepsilon^k_{ij} \mathrm{d}V, \tag{5}$$

$$< \sigma^k_{ij} > = \frac{1}{V} \int_\Omega \sigma^k_{ij} \mathrm{d}V, \tag{6}$$

where Ω is the domain of volume V that represents the probed sample and $k = 1, 2, 3$ denotes the kth oscillatory test described above and illustrated in Figures 2a–2c, respectively.

Under plane strain conditions and assuming that the responses of the probed sample can be represented by an equivalent homogeneous anisotropic viscoelastic solid (Rubino et al., 2016), the average stress and strain components (equations (5) and (6)) can be related through a complex-valued, frequency-dependent equivalent Voigt stiffness matrix

$$\begin{bmatrix} < \sigma^k_{11} > \\ < \sigma^k_{22} > \\ < \sigma^k_{12} > \end{bmatrix} = \begin{bmatrix} C_{11}(\omega) & C_{12}(\omega) & C_{16}(\omega) \\ C_{12}(\omega) & C_{22}(\omega) & C_{26}(\omega) \\ C_{16}(\omega) & C_{26}(\omega) & C_{66}(\omega) \end{bmatrix} \cdot \begin{bmatrix} < \varepsilon^k_{11} > \\ < \varepsilon^k_{22} > \\ < 2\varepsilon^k_{12} > \end{bmatrix}. \tag{7}$$

The structure of the stiffness matrix in equation (7) corresponds to the highest degree of anisotropy for a 2-D sample and holds for the three oscillatory relaxation tests described above. Thus, we have nine equations (equation (7) for $k = 1, 2, 3$) and six unknowns ($C_{ij}(\omega)$ with $i \leq j$). The components of the equivalent stiffness matrix are evaluated for each frequency ω following a classic least squares procedure, as it provides the best representation of the heterogeneous porous rock using an equivalent homogeneous anisotropic viscoelastic solid. Once the coefficients $C_{ij}(\omega)$ are determined, we compute the equivalent phase velocity and attenuation of P and S waves as functions of incidence angle and frequency following a standard procedure for anisotropic viscoelastic solids. It is important to mention that for the 2-D samples considered (Figure 1), we can only compute the seismic velocities and attenuation of the S wave polarized in the plane normal to the fractures surface (in-plane S wave). Accordingly, we can only compute the P wave anisotropy in the plane normal to the fractures.

Table 1
Physical Properties of the Materials Employed in the Numerical Analysis

	Background	Fracture
Porosity, ϕ	0.067	0.8
Permeability, κ	1×10^{-5} D	100 D
Solid bulk modulus, K_s	37 GPa	37 GPa
Solid density, ρ_s	2,650 kg/m^3	2,650 kg/m^3
Frame bulk modulus, K_m	–	0.02 GPa
Frame shear modulus, μ_m	–	0.01 GPa
Fluid density, ρ_f	1,090 kg/m^3	1,090 kg/m^3
Fluid shear viscosity, η_f	0.01 Poise	0.01 Poise
Fluid bulk modulus, K_f	2.25 GPa	2.25 GPa

3. Numerical Analysis

3.1. Fracture Network Properties

For this initial analysis, we consider the sample shown in Figure 1, which represents a unit cell of a periodic distribution of two orthogonal fracture sets that are hydraulically connected. The fractures are represented by ellipsoids with major and minor axes (length and aperture) equal to 2 and 0.03 cm, respectively. The side length of the sample is 3.33 cm. The physical properties of the fractures were chosen following Rubino et al. (2014) and are given in Table 1. This simple fracture network model allows us to illustrate the impact of the intrinsic anisotropy on the WIFF effects, especially at the two characteristic regimes of maximal seismic attenuation and phase velocity dispersion. The first regime (FB-WIFF) prevails at relatively low frequencies and is produced by the pressure gradients between the fractures and the background generated by a propagating wave. In order to return to the state of equilibrium, fluid flows between these two regions, which, in turn, produces attenuation and phase velocity dispersion. Given that the FB-WIFF characteristic frequency is primarily controlled by the diffusivity of the background and the geometry and distribution of fractures (Guo et al., 2016), we can easily illustrate the changes on FB-WIFF effects exclusively due to the background anisotropy by considering the fractures distribution in Figure 1.

On the other hand, as found by Rubino et al. (2013), the second regime (FF-WIFF) prevails when the propagating wave induces a fluid pressure gradient between connected fractures. As a consequence, energy dissipation occurs during the corresponding fluid pressure equilibration. As pointed out by Rubino et al. (2014), FF-WIFF can be regarded as the mesoscopic analogue of the squirt flow mechanism. Guo et al. (2016) found that the FF-WIFF characteristic frequency depends on the geometrical properties of the fracture network and on an effective diffusivity of the rock. The latter corresponds to the diffusivity of an effective medium where the fractures parallel to the wave propagation and the saturated background act as the pore space and the solid phase, respectively. As for the case of FB-WIFF, considering a single-fracture geometry simplifies the analysis.

3.2. Intrinsic Anisotropy Parameterization

For simplicity, the background rock is represented as a transversely isotropic medium whose symmetry axis is aligned with the x_2 axis (VTI). Although our methodology allows us to consider an elastically anisotropic background with lower symmetry, we chose a VTI background as it represents a common and realistic scenario.

Furthermore, we assume that the saturated-frame stiffness coefficients C^s_{ij} of the background can be related to the dry-frame stiffness coefficients C^d_{ij} through the anisotropic Gassmann (1951) equations

$$C^s_{ij} = C^d_{ij} + \alpha_i \alpha_j M \qquad i,j = 1, \ldots 6, \tag{8}$$

where, for a VTI medium, the dry stiffness matrix has the form

$$\mathbf{C}^d = \begin{bmatrix} C^d_{11} & C^d_{12} & C^d_{13} & 0 & 0 & 0 \\ C^d_{12} & C^d_{22} & C^d_{12} & 0 & 0 & 0 \\ C^d_{13} & C^d_{12} & C^d_{11} & 0 & 0 & 0 \\ 0 & 0 & 0 & C^d_{66} & 0 & 0 \\ 0 & 0 & 0 & 0 & C^d_{55} & 0 \\ 0 & 0 & 0 & 0 & 0 & C^d_{66} \end{bmatrix}. \tag{9}$$

The coefficients α_m are

$$\alpha_m = 1 - \frac{\sum_{n=1}^{3} C^d_{mn}}{3K_g} \qquad m = 1,2,3, \tag{10}$$

Table 2
C_{ij}^d Coefficients and Thomsen Parameters Considered in the Numerical Analysis of Elastic Anisotropy

	Isotropic case	Anisotropic case
C_{11}	46.9 GPa	47.31 GPa
C_{22}	46.9 GPa	33.89 GPa
C_{66}	21.13 GPa	17.15 GPa
C_{12}	4.64 GPa	5.29 GPa
C_{55}	21.13 GPa	19.74 GPa
C_{13}	4.64 GPa	7.83 GPa
ε	0	0.198
δ	0	0.197

Note. The values correspond to the sample G16 of Wang (2002).

$\alpha_4 = \alpha_5 = \alpha_6 = 0$, and the scalar M is

$$M = \frac{K_g}{(1 - \frac{K^*}{K_g}) - \phi(1 - \frac{K_g}{K_f})}. \tag{11}$$

In equations (10) and (11), ϕ is the porosity, K_g the grain solid bulk modulus, K_f the pore fluid bulk modulus, and K^* is the generalized drained bulk modulus defined as

$$K^* = \frac{1}{9}\sum_{i=1}^{3}\sum_{j=1}^{3} C_{ij}^d. \tag{12}$$

Equations (8) to (12) reduce to the isotropic Gassmann (1951) relations in the case of the poroelastic medium representing the fractures.

Notice that even though this methodology is implemented for 2-D samples and we only need the stiffness matrix shown in equation (4) to define the seismic wave propagation in the x_1-x_2 plane, in order to obtain these stiffness elements we must define the full stiffness matrix of the dry background. For the numerical analysis, we use C_{ij}^d coefficients computed from the velocity measurements done by Wang (2002) in tight sandstones with air inside the pores. By proceeding this way, we ensure that both the stiffness coefficients and the degree of anisotropy are realistic. Wang (2002) performed measurements at different net reservoir pressures, thus obtaining different degrees of anisotropy and C_{ij}^d coefficients for a given sample. We chose the sample that presented the largest anisotropy variation when subjected to the different pressure conditions. The dry stiffness matrix corresponding to the condition of maximal anisotropy is used to represent the anisotropic background scenario. We arbitrarily define the dry stiffness matrix for the isotropic reference scenario by making its dry P wave and shear moduli equal to the values of C_{22}^d and C_{55}^d, respectively, corresponding to the condition of minimal anisotropy of the sample. The stiffness coefficients for both cases are given in Table 2 along with the computed Thomsen (1986) parameters. It is important to mention that, although we consider frequency-independent stiffness coefficients in equation (9), this methodology naturally permits to account for complex-valued and frequency-dependent background stiffness coefficients due to the fact that the relaxation tests are performed in the space-frequency domain. The rest of the physical properties necessary for the numerical analysis are given in Table 1.

The hydraulic anisotropy of the background is characterized by a permeability tensor. For this work, we consider a diagonal permeability tensor defined as

$$\boldsymbol{\kappa} = \begin{bmatrix} \kappa_1 & 0 & 0 \\ 0 & \kappa_2 & 0 \\ 0 & 0 & \kappa_1 \end{bmatrix}. \tag{13}$$

Although more complex scenarios can be considered, in many, if not most, cases the diagonal elements of the permeability tensor are more significant than the nondiagonal ones (Rasolofosaon & Zinszner, 2002). For the hydraulic anisotropy sensitivity analysis, we consider different anisotropy scenarios by varying the ratio κ_1/κ_2.

3.3. Results

In the following, we study the impact of the elastic and hydraulic anisotropy of the background on the effective elastic properties of a fractured rock. To this end, we consider four scenarios with varying background anisotropy: (i) isotropic reference; (ii) elastically anisotropic; (iii) hydraulically anisotropic; and (iv) both elastically and hydraulically anisotropic. By proceeding this way, we can better identify and assess the effects due to the different types of intrinsic anisotropy of the background.

3.3.1. Isotropic Background Reference Scenario

Given that WIFF effects depend on both the background and the fracture network properties, the case of an isotropic background is presented as a reference scenario. This allows us to illustrate the characteristics of the WIFF effects on the seismic properties related to the fracture network considered and hence, to better understand their sensitivity to the intrinsic anisotropy of the background rock. The physical properties used for the numerical analysis of the isotropic background are detailed in Tables 1 and 2.

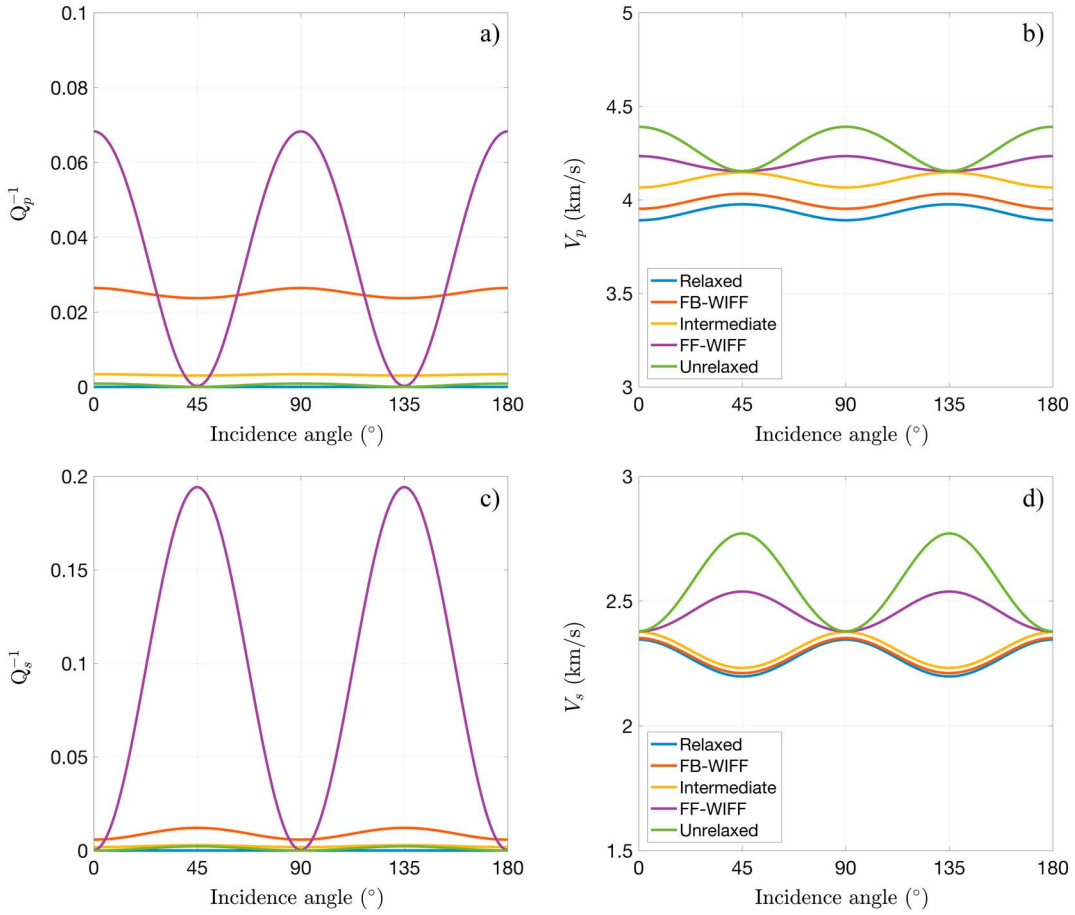

Figure 3. (a, b) *P* and (c, d) *S* wave attenuation (Figures 3a and 3c) and phase velocity (Figures 3b and 3d) for a fractured sample with isotropic background as functions of angles of incidence at different WIFF regimes.

Figure 3 shows the angle dependence of the *P* and *S* wave phase velocity and attenuation for five WIFF regimes: (i) relaxed (low-frequency limit), (ii) FB-WIFF peak, (iii) intermediate plateau, (iv) FF-WIFF peak, and (v) unrelaxed regime (high-frequency limit). Notice that we refer to the frequency regime between the FB-WIFF and FF-WIFF peaks where attenuation and velocity dispersion are minimal as the intermediate plateau. The incidence angle is measured with respect to the vertical axis.

As expected for an isotropic background and due to the characteristics of the fractures, the *P* and *S* wave phase velocity and attenuation values at vertical and horizontal incidence turn out to be exactly the same (Figure 3). In addition, we observe that WIFF effects produce frequency-dependent effective velocity anisotropy. However, the most prominent feature in Figure 3 is that the polarity of both the *P* and *S* wave velocity anisotropy is not the same for all frequencies. Although this result is related to the presence of orthogonal fractures, a similar behavior has been observed for aligned cracks or fractures by other authors (e.g., Collet & Gurevich, 2016; Galvin & Gurevich, 2015).

The changes in the polarity of the phase velocity anisotropy are related to the effective frequency-dependent mechanical compliance of the fractures. This implies that, although fractures always softens a rock, the effective anisotropy becomes frequency dependent. Let us first consider the *P* wave phase velocity anisotropy. In the relaxed regime, there is time for fluid to flow in or out of the fractures and the stiffening effect of the fluid saturating the fracture is minimal. The maximal deformation of fractures is associated with compression normal to their surfaces. In the case of two orthogonal fractures, this implies that at vertical and horizontal incidence the phase velocity is at its minimum, whereas at an incidence angle of 45° the phase velocity reaches its maximum. As the frequency increases, there is less time for fluid to flow between the fractures and the background and the pressure inside the fractures increase. Hence, the stiffening effect of the fluid inside the fractures becomes more significant. In the unrelaxed regime, this stiffening effect is maximal as there is

no time for fluid pressure communication between fractures and background as well as between connected fractures. This implies that the maximal deformation of a given fracture will not occur normal to the fractures surface but close to 45° incidence where the influence of the tangential compliance of the fractures is still significant (Collet & Gurevich, 2016). Consequently, the velocity anisotropy shows a different polarity compared to the relaxed regime.

Interestingly, we observe in Figure 3b that at frequencies corresponding to the intermediate plateau and higher, the *P* wave phase velocity at 45° does not increase with frequency anymore, as it does for vertical and horizontal incidence. Consequently, there is a given frequency for which, $V_P(45°) = V_P(0°) = V_P(90°)$ and the *P* wave phase velocity is virtually isotropic. These results are in agreement with the findings of Rubino et al. (2017) who showed that the level of phase velocity anisotropy produced by the presence of fractures is strongly affected by the degree of hydraulic connectivity of the fracture network. Moreover, they found that, in the case of low-permeability formations and fully connected fractures, the regime where $V_P(45°) \sim V_P(0°) \sim V_P(90°)$ prevails in the seismic frequency band.

The magnitude and anisotropy of the *P* wave attenuation shown in Figure 3a is, as expected, only significant in the FB-WIFF and FF-WIFF regimes. In both regimes, maximal attenuation occurs at horizontal and vertical incidence, as the fluid pressure gradient is maximal for these directions of wave propagation.

The velocity anisotropy of the in-plane polarized *S* wave also exhibits a change in polarity with frequency, but, in this case, the maximal phase velocity dispersion occurs close to 45°. This is due to the fact that, at oblique incidence, the *S* wave phase velocity is affected by the normal compliance of both fractures. At vertical and horizontal incidence, on the other hand, the *S* wave phase velocity has almost no dispersion as it is mainly controlled by the tangential compliance of the fractures, whose frequency dependence is negligible. As the normal compliance of the fractures is significant in the relaxed regime, the velocity is at its minimum for ∼45°. However, as the frequency increases, the normal compliance of the fractures gets larger due to the stiffening effect of the fluid and reaches its maximum in the unrelaxed regime, where the velocity at oblique incidence can be larger than at vertical and horizontal incidence (Figure 3d).

We observe that for any frequency regime, at vertical and horizontal *S* wave incidence, the corresponding attenuation is negligible as *S* waves propagating normal or parallel to the fractures do not influence significantly the fluid pressure inside the fractures. The maximal *S* wave attenuation occurs at an angle of incidence of ∼45°, and it is particularly strong in the FF-WIFF regime. As pointed out by Rubino et al. (2017), this is related to the fact that the induced pressures are positive and negative in the horizontal and vertical fractures, respectively, and hence, the fluid pressure gradient between connected fractures is particularly large.

Lastly, it is possible to link the change in polarity of the velocity anisotropy to the parameters derived by Thomsen (1986). For weak anisotropy, the angle dependence of the *P* and *S* waves phase velocity are given by

$$\begin{aligned} V_P(\theta) &\approx V_P(0°)(1 + \delta \sin^2(\theta)\cos^2(\theta) + \epsilon \sin^4(\theta)), \\ V_S(\theta) &\approx V_S(0°)(1 + \frac{V_P^2(0°)}{V_S^2(0°)}(\epsilon - \delta)\sin^2(\theta)\cos^2(\theta)), \end{aligned} \tag{14}$$

where θ denotes the incidence angle and the Thomsen (1986) anisotropy parameters are

$$\begin{aligned} \epsilon &= \frac{C_{11} - C_{22}}{2C_{22}}, \\ \delta &= \frac{(C_{12} + C_{66})^2 - (C_{22} - C_{66})^2}{2C_{22}(C_{22} - C_{66})}. \end{aligned} \tag{15}$$

Although some discrepancies are to be expected for strong anisotropy, equation (14) shows that the angle dependence of the wave velocities is controlled by δ and ϵ. For the case of orthogonal fractures embedded in an isotropic background, we have $\epsilon = 0$ ($C_{11} = C_{22}$) and the velocity anisotropy depends exclusively on δ. Indeed, the coefficient δ provides the exact second derivative of *P* wave phase velocity at vertical incidence (Tsvankin, 1997). Hence, the polarity of the *P* wave phase velocity anisotropy can be related to positive and negative regimes of δ. From the results shown in Figure 3, the positive and negative regimes of δ coincide with the low- and high-frequency regimes, respectively. It is important to notice that in the case of *S* waves, the polarity of the velocity anisotropy has opposite sign with respect to δ (equation (14)).

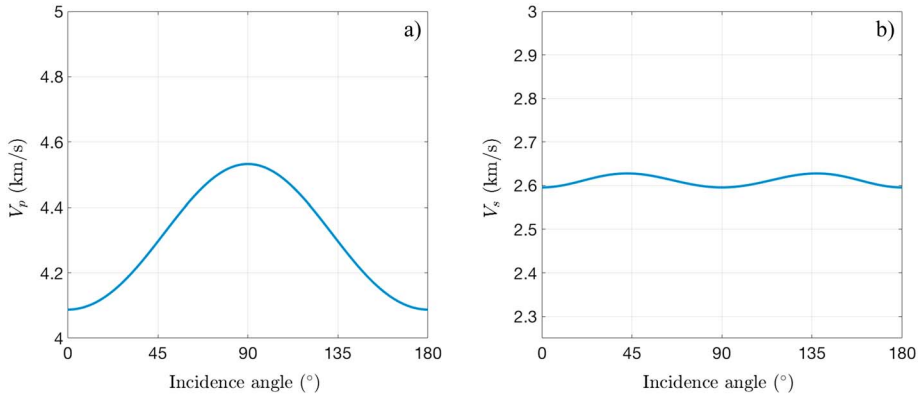

Figure 4. (a) *P* and (b) *S* wave phase velocity as functions of incidence angle for an unfractured anisotropic background whose stiffness elements are given in Table 2.

3.3.2. Sensitivity to the Elastic Anisotropy of the Background

For the numerical analysis of elastic anisotropy, we use the C_{ij}^{d} coefficients given in Table 2 that correspond to the anisotropic case. The other physical properties are given in Table 1. Figure 4 shows the *P* and *S* wave velocity anisotropy corresponding to the unfractured anisotropic background fully saturated with brine. We observe that, in the x_1-x_2 plane, the angle dependence of the *P* wave phase velocity is more pronounced than that for the *S* wave. This is due to the fact that for VTI media and in the x_1-x_2 plane, the in-plane polarized *S* wave velocity anisotropy is mainly controlled by the anellipticity of the medium (equation (14)). As the anisotropy of the background is close to the elliptical condition ($\delta = \epsilon$), the velocity anisotropy of the in-plane *S* wave is weak.

Figure 5 shows the *P* wave velocity and attenuation as functions of frequency at vertical and horizontal directions of propagation for a sample containing orthogonal fractures (Figure 1). We can clearly observe that in the presence of moderate background elastic anisotropy, the *P* wave attenuation and velocity dispersion are different for horizontal and vertical incidence. Given that C_{11}^{s} is greater than C_{22}^{s}, the velocities at horizontal incidence are higher than at vertical incidence. For both FB-WIFF and FF-WIFF manifestations, the higher attenuation peak at horizontal incidence compared to vertical incidence is explained by the fact that a larger compressibility contrast between the fractures and the background increases the fluid pressure gradient between these two regions.

Interestingly, the FB-WIFF characteristic frequency is approximately the same for both directions of propagation. As far as we know, there are no expressions for the FB-WIFF characteristic frequency for the case of an elastically anisotropic background. For an isotropic background, Guo et al. (2016) found that this characteristic frequency can be computed as

$$f_{\mathrm{FB}} = \frac{2D_b}{a_f^2}, \tag{16}$$

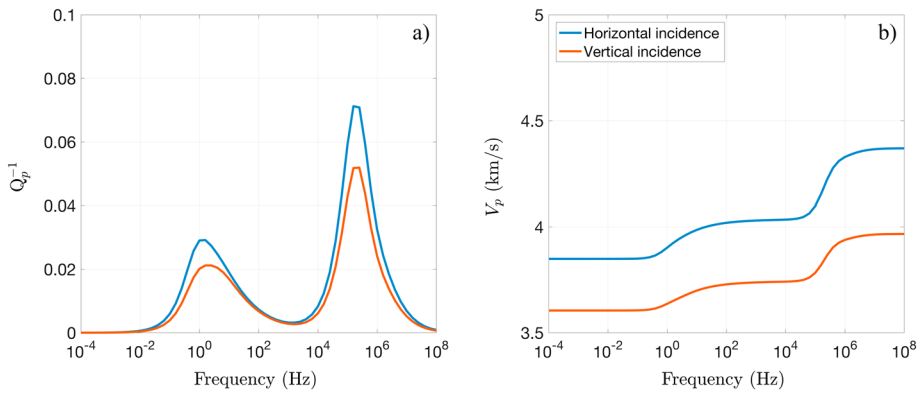

Figure 5. (a) *P* wave attenuation and (b) phase velocity at vertical and horizontal incidence as functions of frequency.

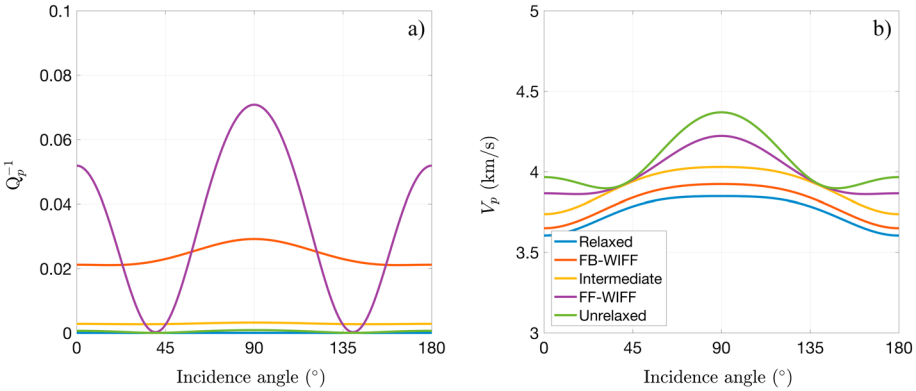

Figure 6. (a) *P* wave attenuation and (b) phase velocity as functions of angles of incidence at different WIFF regimes for a fractured rock in the presence of elastic intrinsic anisotropy.

where a_f is the fracture length and D_b is the diffusivity of the background that is computed as

$$D_b = \frac{M_b L_b \kappa_b}{\eta C_b}, \tag{17}$$

with M_b, L_b, and C_b being the pore space modulus, and the dry and saturated *P* wave moduli of the background medium, respectively. We can approximate the diffusivity in the anisotropic case by computing M_b with equation (11) and L_b and C_b as

$$\begin{aligned} L_b &= \frac{C_{11}^d + C_{22}^d + C_{33}^d}{3}, \\ C_b &= \frac{C_{11}^s + C_{22}^s + C_{33}^s}{3}. \end{aligned} \tag{18}$$

By using equation (16) with the approximated effective diffusivity of the background, we find that f_{FB} is equal to 1.03 Hz, which is reasonably close to the observed characteristic frequency. However, for stronger anisotropies, such as in the case of shales or coals, the shift in the FB-WIFF characteristic frequency for different incidence angles may be more pronounced and, hence, a more general expression for f_{FB} may be required.

The FF-WIFF characteristic frequency also coincides for the two angles of incidence considered, which implies that it is mainly controlled by the fracture parameters. The difference in attenuation magnitude is explained by the different compressibility contrasts at vertical and horizontal directions of propagation. A larger compressibility contrast produces a larger pressure gradient between the connected fractures and, hence, more pronounced FF-WIFF effects.

The intrinsic elastic anisotropy of the background has a first-order impact on the *P* wave attenuation and the angle dependence of the velocity (Figure 6). In the low-frequency regime of the velocity anisotropy ($\delta > 0$), the *P* wave phase velocity minimum observed at 90° incidence for an isotropic background is not observed when the background is intrinsically anisotropic. Instead, the VTI nature of the background dominates the angle dependence of the velocity. In this regime, the attenuation is only significant at frequencies close to the FB-WIFF peak. The *P* wave attenuation increases for close to horizontal directions of propagation as the background gets stiffer in this direction, and thus, the contrast with respect to the fracture properties is strongest. Hence, while for an isotropic background, the angle dependence of the attenuation follows a $\cos(4\theta)$ periodicity (Figure 3), the angle dependence observed in Figure 6 tends to a $\cos(2\theta)$ periodicity for strong intrinsic anisotropy.

In the high-frequency regime of velocity anisotropy (δ <0), both the influence of the intrinsic anisotropy of the background and the stiffening effect of the fluid in the fractures are significant. In the unrelaxed limit, the relatively low mechanical compliance of the fractures produces *P* wave phase velocities at horizontal and vertical incidence that are close to those of the unfractured background. At incidence angles close to 45°, and due to the influence of the tangential compliance of the fractures, the *P* wave velocity has a minimum. The attenuation anisotropy, on the other hand, is important at frequencies in the FF-WIFF regime, and is significantly

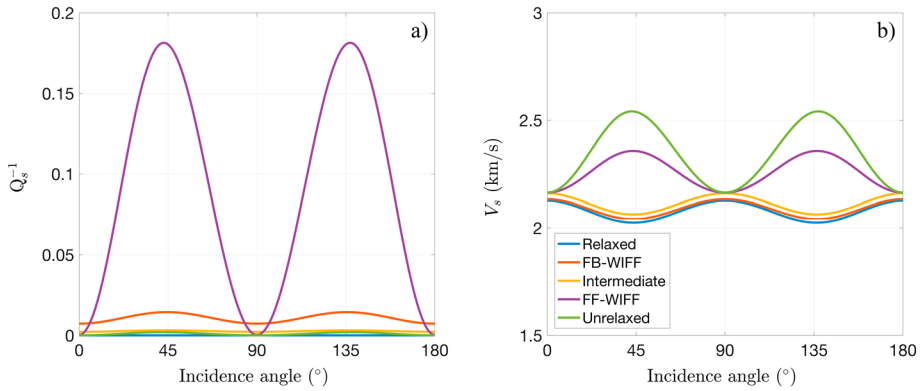

Figure 7. (a) *S* wave attenuation and (b) phase velocity as functions of angles of incidence at different WIFF regimes for a fractured rock in the presence of elastic intrinsic anisotropy.

higher than in the FB-WIFF regime. The magnitude of the attenuation is at its maximum at horizontal *P* wave propagation as the compressibility contrast between the fractures and the background is larger in this direction. At 45° incidence, the FF-WIFF attenuation is close to zero for a purely isotropic background due to the negligible fluid pressure gradient between the fractures (Figure 3). In the case of an intrinsically anisotropic background, the angle at which this minimum occurs is slightly shifted toward the vertical (Figure 6). This is due to the fact that $C^s_{22} < C^s_{11}$, and hence, an angle closer to the x_2 direction is needed in order to induce similar pressure gradients inside both fractures.

Figure 7 shows the *S* wave phase velocity and attenuation as functions of the angle of incidence, at the same five WIFF regimes as shown in Figure 6. As the in-plane polarized *S* wave velocity anisotropy of the background is relatively weak (Figure 4), the corresponding velocity and attenuation anisotropy in the fractured sample is mainly controlled by the orientation of the fractures and, hence, similar to that shown in Figure 3 for an isotropic background. As for *P* waves, we observe that, as a consequence of the intrinsic elastic anisotropy of the background, the angle at which the maximal velocity dispersion and attenuation occur is slightly shifted from 45°.

Lastly, in order to quantify the effective anisotropy of the medium, we compute the anisotropy parameters ϵ and δ defined in equation (15). Figure 8 shows the real components of ϵ and δ as functions of the frequency, which are related to the *P* and *S* wave velocity anisotropy (Collet & Gurevich, 2016). The reference values of ϵ and δ for the saturated unfractured background are 0.1148 and 0.0913, respectively. We observe that the intrinsic anisotropy of the background produces a frequency dependence of ϵ. As mentioned above, for an isotropic background and due to the fracture distribution, ϵ is zero. However, in the presence of elastic anisotropy in the background, ϵ increases with frequency and approaches a value close to that corresponding to the unfractured background in the unrelaxed limit. On the other hand, δ shows that the above mentioned positive and negative regimes prevail at low and high frequencies, respectively. As for the case of an isotropic background, the sign of δ is related to the polarity of the velocity anisotropy (equation (14)).

3.3.3. Sensitivity to Hydraulic Anisotropy of the Background

Here we explore the effective properties of fractured rocks in the presence of permeability anisotropy of the background. To do so, we use the background permeability tensor given by equation (13) considering different relations between κ_1 and κ_2. The vertical permeability κ_2 is kept constant and equal to 1×10^{-5} D, while we change the horizontal permeability κ_1. We consider two scenarios given by κ_1/κ_2 equal to 10 and 100. Although $\kappa_1/\kappa_2 = 100$ may be unrealistically large, this scenario is considered to enhance and illustrate the effects of hydraulic anisotropy of the background. The mechanical properties of the background are assumed to be isotropic (Table 2) and the rest of the physical properties are given in Table 1.

Figure 9 shows the *P* wave phase velocity and attenuation as functions of frequency at vertical and horizontal incidence for the two scenarios of permeability anisotropy mentioned above. By comparing the top ($\kappa_1 = 10\kappa_2$) and bottom ($\kappa_1 = 100\kappa_2$) panels in Figure 9, it is clear that the intrinsic hydraulic anisotropy of the background only modifies the fluid pressure relaxation process between the fractures and background.

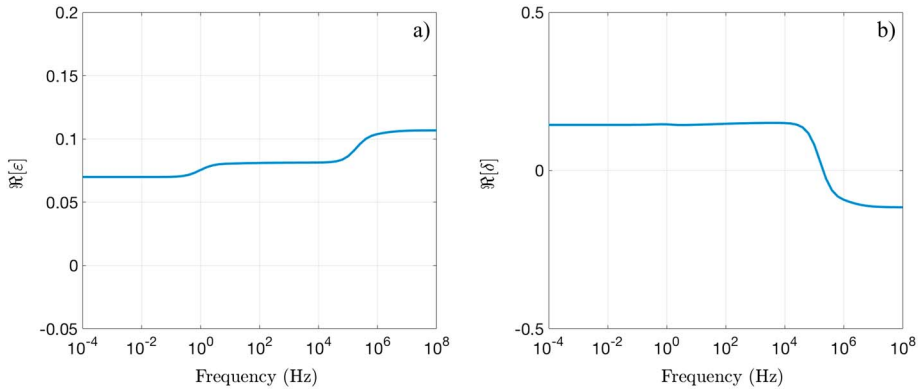

Figure 8. Real component of the Thomsen parameters (a) ϵ and (b) δ as functions of frequency in the presence of intrinsic elastic anisotropy.

That is, the effective seismic response at the relaxed and unrelaxed limits as well as the FF-WIFF process are not affected by the permeability of the background. The relaxed limit is not affected as in the low-frequency limit there is sufficient time for fluid to flow from the fractures to the background regardless of the permeability of the background. On the other hand, the FF-WIFF, and unrelaxed regimes are not affected by the hydraulic

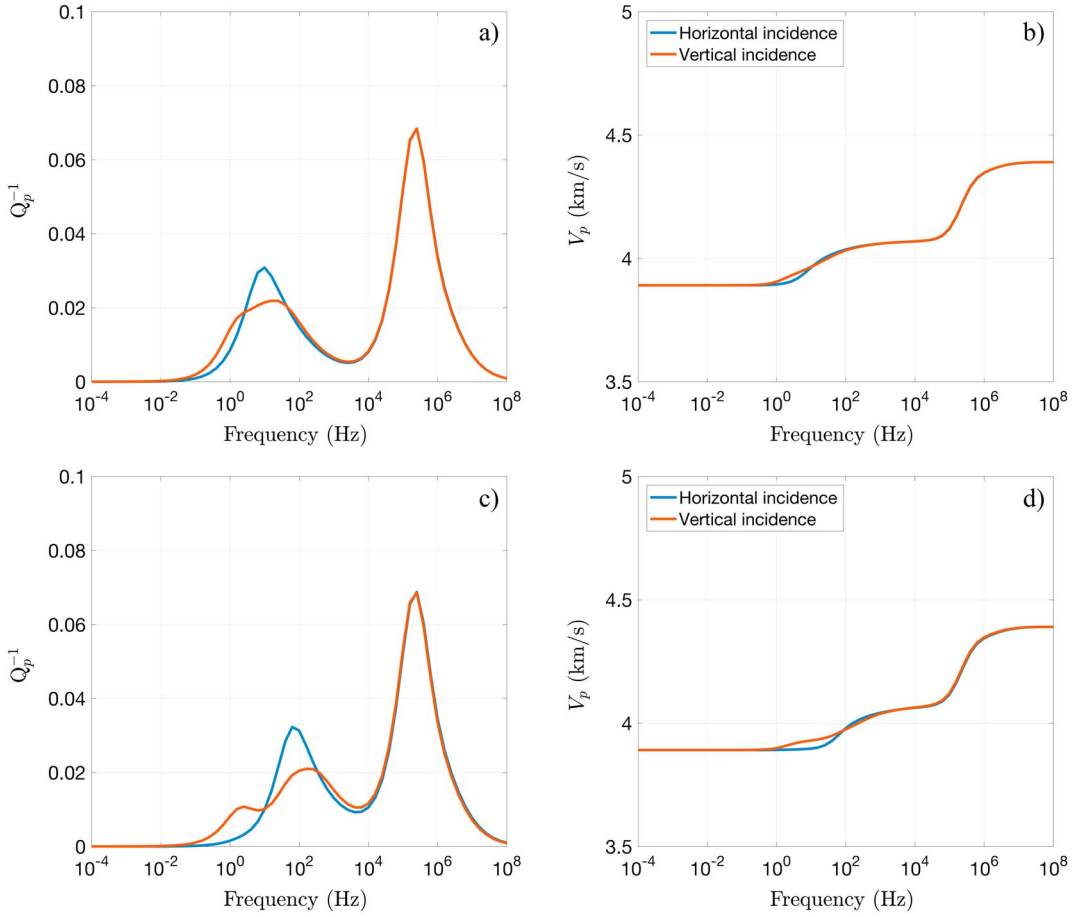

Figure 9. (a, c) *P* wave attenuation and (b, d) phase velocity at vertical and horizontal incidence as functions of frequency. Permeability in the vertical direction κ_2 is equal to 1×10^{-5} D, while the horizontal permeability κ_1 is equal to $10\kappa_2$ (Figures 9a and 9b) and $100\kappa_2$ (Figures 9b and 9d).

anisotropy of the background as at these relatively high frequencies the fractures are hydraulically isolated with respect to the background.

The most significant effects of the background hydraulic anisotropy occur in the FB-WIFF regime, where both the characteristic frequency and magnitude of the attenuation and velocity dispersion are angle dependent. The velocity dispersion and attenuation are sharper when the wave propagates in the horizontal direction, that is, parallel to the direction of maximal background permeability (κ_1). In the direction of minimal permeability (κ_2), on the other hand, the curves are flatter and exhibit two FB-WIFF peaks. By comparing the two permeability anisotropy scenarios at vertical incidence, we notice that the separation between the characteristic frequencies of the two FB-WIFF peaks increases with increasing hydraulic anisotropy. Moreover, the ratio between these two characteristic frequencies is approximately given by the ratio κ_1/κ_2. This suggests that the lower FB-WIFF characteristic frequency is related to the minimum permeability and the higher one to the maximum background permeability. Indeed, the vertical *P* wave propagation attenuation shows that the lower FB-WIFF characteristic frequency remains unchanged for the two permeability anisotropy scenarios considered, which is due to the fact that κ_2 does not change. Conversely, the higher one shifts by 1 order of magnitude when varying κ_1 1 order of magnitude.

To further analyze this angle dependence of the FB-WIFF effects, we compute the fluid pressure fields and the *P* wave inverse quality factor density (Appendix A) for the horizontal and vertical relaxation tests. The latter illustrates the energy dissipation patterns for horizontal and vertical directions of *P* wave propagation, respectively and, hence, is helpful for exploring the underlying fluid pressure diffusion process at different frequencies. We include the real component of the fluid pressure fields normalized by the mean fluid pressure in the sample for completeness as, according to equation (A2), strong energy dissipation will occur in the regions of strong fluid pressure gradients. Figure 10 shows the inverse quality factor density (Figures 10a, 10c, and 10e) and normalized fluid pressure field (Figures 10b, 10d, and 10f) for the vertical (Figures 10a, 10b, 10e, and 10f) and horizontal (Figures 10c and 10d) relaxation tests for $\kappa_1 = 100\kappa_2$. For illustration purposes, we analyze these attributes at the frequencies associated with the peaks of the FB-WIFF *P* wave attenuation. Hence, the first and third rows in Figure 10 correspond to the lower ($f \sim 2.5$ Hz) and higher ($f \sim 250$ Hz) FB-WIFF characteristic frequencies observed at vertical incidence for $\kappa_1 = 100\kappa_2$. The second row corresponds to the single FB-WIFF characteristic frequency ($f \sim 65$ Hz) observed at horizontal incidence (Figure 9) for the same permeability anisotropy.

We observe that the energy dissipation in the FB-WIFF regime occurs mainly in the immediate vicinity of the fractures. The panels in the first and second rows in Figure 10 illustrate the classical interpretation of FB-WIFF. At this frequency, strong fluid pressure gradients occur normal to the fractures surface (Figures 10b and 10d), which induces the fluid flow between fractures and background. The fluid exchange between the two regions produces the energy dissipation areas covering the total length of the fractures that we observe in Figures 10a and 10c. In addition, the energy dissipation areas expand in the horizontal direction as this direction represents a preferential path for the fluid flow between the fractures and background due to $\kappa_1/\kappa_2 \gg 1$. Notice that in the case of a hydraulically isotropic background and due to the symmetry of the fracture network, the characteristic frequencies at vertical and horizontal incidence would be the same. However, this is not the case in the presence of hydraulic anisotropy in the background. In the particular case considered here, the FB-WIFF characteristic frequency at horizontal incidence lies between the two characteristic frequencies observed at vertical incidence (Figure 9c). This, in turn, indicates that the FB-WIFF characteristic frequency at horizontal incidence is related to an averaged permeability given by both the horizontal and vertical permeabilities.

Figures 10e and 10f show the plots corresponding to the lower FB-WIFF characteristic frequency observed only at vertical incidence (Figures 9). At this lower frequency, the pressure gradients in the vicinity of the fractures have enough time during a wave cycle to equilibrate except in the region close to the tips of the vertical fracture (Figure 10f). This is due to the fact that for the amount of time included in a wave half cycle, the lower vertical background permeability κ_2 acts as a barrier for the fluid pressure diffusion at the tips of the vertical fracture, thus increasing the fluid pressure gradient in this region of the background. As a consequence, some energy dissipation takes place at the tips of the vertical fracture (Figures 10e). The energy dissipation region is elongated in the direction of the maximal permeability, following the fluid pressure barrier observed in Figure 10f. This phenomenon manifests itself as an additional attenuation peak and velocity dispersion step at lower frequencies. In the horizontal direction of *P* wave propagation, on the other hand, this phenomenon

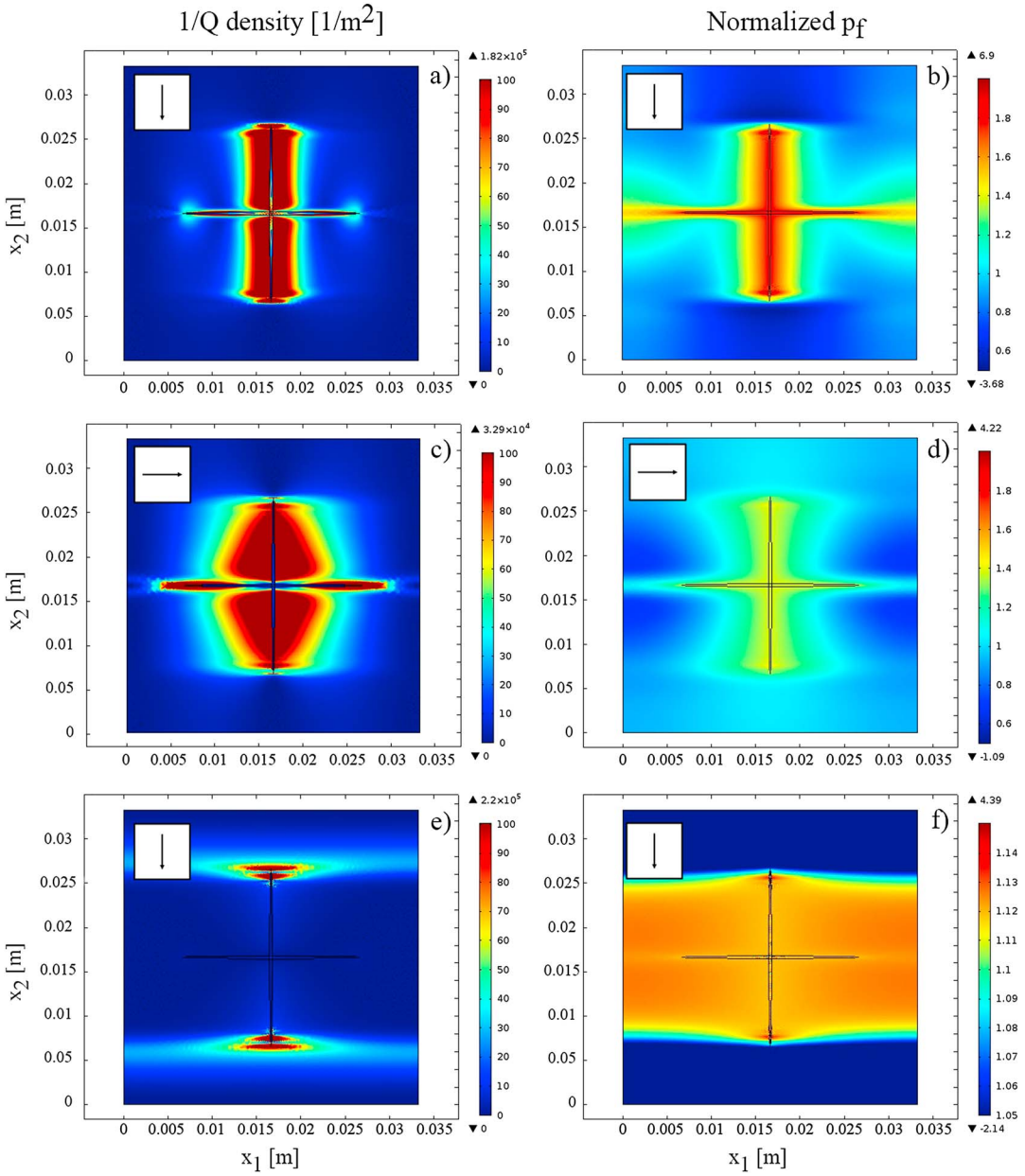

Figure 10. (left column) *P* wave inverse quality factor density and (right column) fluid pressure for the (a, b, e, f) vertical and (c, d) horizontal relaxation tests in the case that $\kappa_1 = 100\kappa_2$. Figures 10a, 10b, 10e, and 10f correspond to the lower and higher FB-WIFF characteristic frequencies observed at vertical incidence. Figures 10c and 10d correspond to the single FB-WIFF characteristic frequency observed at horizontal incidence. The arrows in the top left corner of the plots illustrate the *P* wave propagation direction.

does not prevail. In this case, the strong fluid pressure gradients are mainly horizontal and the fluid pressure diffusion process at the tips of the horizontal fracture is dominated by κ_1. Hence, the permeability barrier created by κ_2 does not play a significant role. It is important to notice that the manifestation of this additional FB-WIFF peak at different directions of wave propagation does not only depend on the background hydraulic anisotropy but also on the size, orientation, and hydraulic connectivity of the fractures.

The in-plane polarized *S* wave phase velocity and attenuation exhibits a similar behavior as in the case of *P* waves. Figure 11 shows the *S* wave attenuation and phase velocity as functions of frequency for incidence angles of 0° and 45°. As for *P* waves, if κ_2 is kept constant, the FB-WIFF characteristic frequency changes

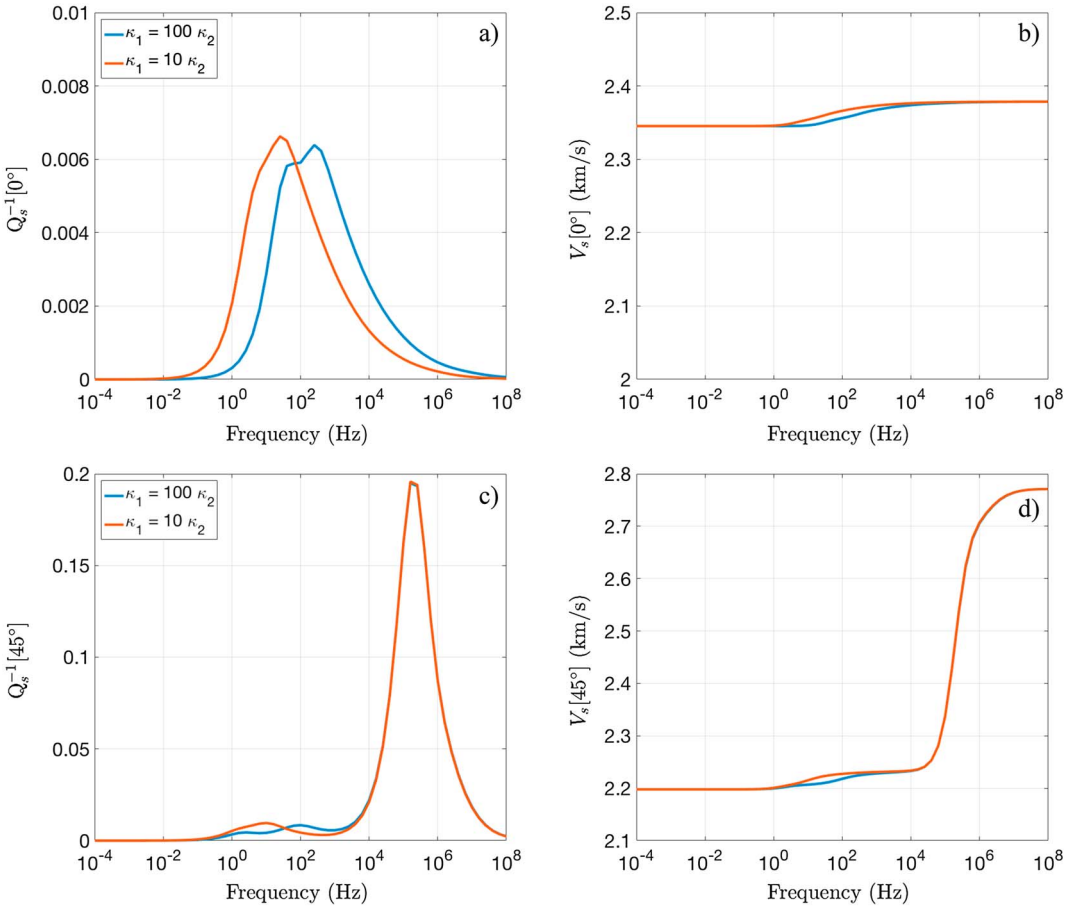

Figure 11. (a, c) *S* wave attenuation and (b, d) phase velocity as functions of frequency at angles of incidence of 0° (Figures 11a and 11b) and 45° (Figures 11c and 11d). Permeability in the vertical direction κ_2 is equal to 1×10^{-5} D, while the horizontal permeability κ_1 is equal to $10\kappa_2$ and $100\kappa_2$.

with κ_1. The manifestation of the second peak in the FB-WIFF regime also depends on the degree of permeability anisotropy of the background. Figures 11c and 11d clearly show that at 45° incidence angle, FF-WIFF attenuation and velocity dispersion are much larger than the effects associated with the FB-WIFF regime, which is in agreement with the results shown in Figure 7.

3.3.4. Hydraulic and Elastic Anisotropy of the Background

For completeness, we consider the combined effects of hydraulic and elastic intrinsic anisotropy of the background. The elastic anisotropy considered in this study corresponds to that given in Table 2. Rasolofosaon and Zinszner (2002) found that the correlation between elastic and hydraulic anisotropy is not always clear. Hence, we explore the cases of the direction of the largest permeability being (i) parallel ($\kappa_1 = 10\kappa_2$) to the direction of largest compressibility contrast between the fractures and background and (ii) perpendicular ($\kappa_1 = 0.1\kappa_2$).

Figure 12 shows the *P* wave attenuation and phase velocity as functions of frequency for the two scenarios presented above. We plot the results for vertical and horizontal wave propagation. As expected from the previous analyses, the different combinations of elastic and hydraulic anisotropy mainly affect the angle dependence of the seismic attenuation and velocity dispersion in the FB-WIFF regime. In Figures 12a and 12b, we observe that the fact that the maximal compressibility contrast and the maximal permeability are aligned with the horizontal direction, produces more pronounced FB-WIFF effects in this direction than in the vertical one. Thus, increasing the *P* wave attenuation anisotropy and, correspondingly, the angle dependence of the velocity dispersion. Although not shown for brevity, in-plane *S* waves experience a similar behavior in the FB-WIFF regime. However, as for other scenarios considered in this study, the effects of intrinsic background anisotropy are smaller than for *P* waves.

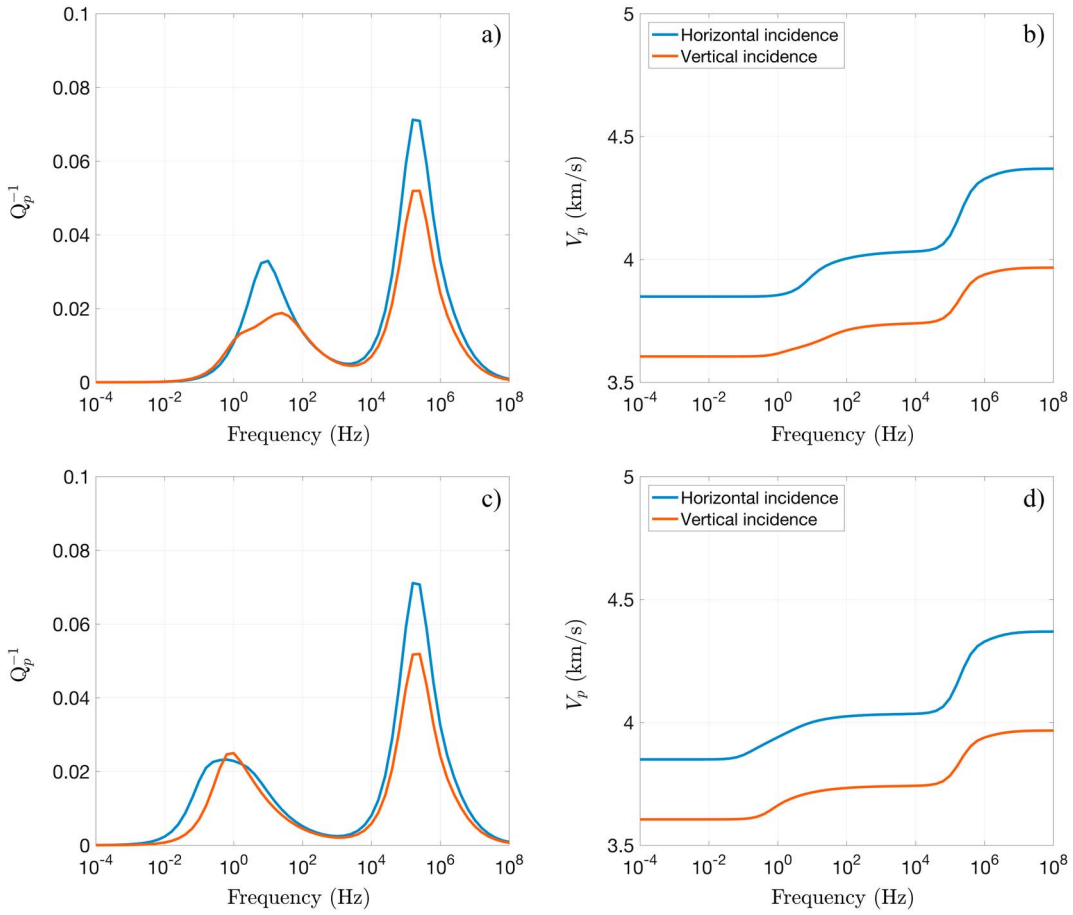

Figure 12. (a, c) *P* wave attenuation and (b, d) phase velocity at vertical and horizontal incidence as functions of frequency. The top and bottom panels correspond to the cases $\kappa_1 > \kappa_2$ and $\kappa_1 < \kappa_2$, respectively.

4. Discussion

An important condition for the validity of this approach is that the intrinsic anisotropy of the background can be modeled by using a homogeneous anisotropic poroelastic medium. This implies that the intrinsic anisotropy considered prevails at the microscale and, hence, can have various origins such as, preferential alignment of fibrous minerals, aligned clay platelets or organic materials, fine layering of materials of different stiffness, aligned microcracks, stress-induced anisotropy effects, for example (e.g., Wang, 2002). In this work, we chose the elastic properties of a tight sandstone reported by Wang (2002) to ensure that the stiffness coefficients and the anisotropy characteristics are realistic and moderate. Although part of this intrinsic anisotropy may be due to the presence of microcracks, squirt flow effects are neglected in the modeling. However, as pointed out by Rubino and Holliger (2013), it is possible to account for squirt flow attenuation due to the presence of fluid-saturated microcracks in the background by allowing the dry frame background stiffness coefficients to be complex valued and frequency dependent. It is also worth noting that although we have used Gassmann's (1951) equations to relate the stiffness coefficients for the dry and saturated frame, a more generic approach may be needed depending on the nature of the considered intrinsic anisotropy. As pointed out by Collet and Gurevich (2016), the anisotropic frame in the case of Gassmann's (1951) equations is assumed to result from preferential alignment of microcracks and grain boundary contacts or layering. Brown and Korringa (1975) have generalized Gassmann's (1951) equations to consider mixed mineralogy and anisotropic minerals.

In this work, we solve Biot (1941) quasi-static consolidation equations in their anisotropic form to infer frequency-dependent seismic properties of fractured porous rocks. Although this study considers a rather complex scenario, the resulting attenuation is purely due to diffusion mechanisms, namely FB-WIFF and FF-WIFF. For illustrative purposes and to analyze the effects of anisotropy on these two diffusion mechanisms,

the parameters are chosen so that the processes are separated in frequency. A drawback of this choice is that, for the physical parameters of the fractures, the quasi-static assumption is violated at high frequencies and additional mechanisms have to be taken into consideration. Sarout (2012) provides a detailed analysis of the frequency ranges for which the quasi-static approximation is valid for a given pore space topology. Mechanisms outside of the validity range include inertia-related effects, such as the development of viscous boundary layers in the pores. Rubino et al. (2014) discusses in detail the rational of fracture conceptualization and the validity of the inferred seismic signatures due to FF-WIFF in the regime of inertial effects. In addition, the considered effective medium approach cannot be applied for frequencies above the scattering frequency associated with the dominant size of the heterogeneities. Milani et al. (2016) explored the errors in the phase velocity and attenuation predicted by a quasi-static model due to neglecting Biot's global flow and scattering effects. For layered media, they found that these effects tend to be important only close to the scattering frequency, for which the effective medium theory is no longer valid.

It is important to note that our numerical approach can be applied to lower background anisotropies and more complex fracture networks. In this initial analysis, we did, however, consider samples containing two sets of orthogonal fractures aligned with the symmetry axis of the VTI background, which corresponds to the most favorable situation for illustrating the impact of the intrinsic anisotropy on the fluid pressure diffusion process along the symmetry directions. By doing so, we have the largest discrepancies in attenuation and phase velocity for horizontal and vertical directions of wave propagation. Although for nonorthogonal fracture intersection the corresponding discrepancies are expected to diminish, the influence of the intrinsic anisotropy on the velocity and attenuation anisotropies will still be significant.

The results shown in this work are based on numerical simulations performed on 2-D samples, which implies that fractures extend infinitely into the third dimension. This suggests that our results overestimate the mesoscopic WIFF effects on the effective seismic properties with respect to those for finite-size fractures. Nevertheless, we found that the attenuation values are comparable to measured values in fractured rocks (e.g., Maultzsch et al., 2007). Furthermore, given that the presence of intrinsic background anisotropy produces a first-order impact on WIFF effects, a similar behavior is expected to prevail for more realistic fracture networks. The extension of the presented methodology to 3-D is conceptually straightforward and will be part of future works.

As stated in section 1, there are numerous effective medium models that describe the dynamic response of fractured rocks due to WIFF in the long-wavelength regime. All these analytical models approximate the effective seismic response by simplifying the problem. Most common approximations are noninteracting fractures, idealized fracture/crack geometries, and a simplified description of the fluid pressure diffusion process. However, provided the corresponding assumptions are reasonably valid for the problem of interest, analytical models can be a powerful tool in inversion schemes to characterize fractured reservoirs, for example, in terms of fracture density, fracture orientation, fracture apertures, and fluid saturation. On the other hand, numerical approaches, such as the one presented in this work, allow for more complex and realistic scenarios, such as, high fracture densities, arbitrary distributions, geometries, and physical properties of fractures, as well as, accurate modeling of the prevailing physical mechanisms. The main drawback of the numerical approach is related to its computational cost, which, in some cases, especially those associated with complex fracture networks, is still prohibitive and makes it unfeasible for inversion schemes.

5. Conclusions

We have adapted a numerical upscaling procedure based on the quasi-static anisotropic poroelastic equations to investigate the role played by the intrinsic anisotropy of the background of fractured media on the characteristics of FB-WIFF and FF-WIFF. To do so, we first defined effective anisotropic viscoelastic solids representing the poroelastic fractured samples of interest. By following a standard procedure for anisotropic viscoelastic solids, we then computed the phase velocity and attenuation of P and S waves as functions of frequency and incidence angle. The main result of this study is that both the intrinsic elastic and hydraulic anisotropy of the background have a significant impact on the angle dependence, the magnitude, and the characteristic frequency of P and S wave seismic attenuation and phase velocity due to WIFF.

We have analyzed the impact of the intrinsic background anisotropy on the physical processes responsible for the seismic anisotropy, attenuation, and velocity dispersion observed. This analysis includes the computation of the inverse quality factor density to explore the role played by the hydraulic anisotropy on the angle

dependence of the fluid pressure diffusion process between the fractures and the background. Interestingly, we found that the presence of hydraulic anisotropy in the background can distort the fluid pressure gradients in the background creating additional manifestations of FB-WIFF depending on the direction of wave propagation. Although not shown for brevity, the corresponding effect can be thought of as that associated with an additional low-permeability layer in the background parallel to the direction of lower background permeability.

The aim of this contribution is to show that FB-WIFF and FF-WIFF can be significantly affected by the presence of intrinsic anisotropy in the background. Given that the intrinsic anisotropy of the background is a rather common feature in fractured environments, including its effects into models used in inversion schemes, is desirable for a correct characterization. Analytical models based on the linear slip theory, such as the one derived by Guo et al. (2016), seem to be suitable for incorporating the effects related to intrinsic background anisotropy.

Appendix A: Inverse Quality Factor Density

To compute the inverse quality factor density for the relaxation tests, we follow the energy-based approach described in Solazzi et al. (2016). By doing so, the local contribution to the inverse quality factor per unit area can be written as

$$q_{kl}^{-1}(\omega) = \frac{< \Delta P(\omega)_{kl} >}{2\omega\delta_{kl} < W(\omega) >}, \tag{A1}$$

where δ_{kl} is the surface of a given computational cell Ω_{kl}. The dissipated power averaged over one wave cycle is given by

$$< \Delta P(\omega)_{kl} > = -\frac{1}{2}\Re\left[\dot{\mathrm{w}}^* \cdot \nabla p_f\right]_{kl}\delta_{kl}, \tag{A2}$$

and the average strain energy at the same computational cell is given by

$$< W(\omega)_{kl} > = \frac{1}{4}\Re\left[\sigma_{11}\varepsilon_{11}^* + \sigma_{22}\varepsilon_{22}^* + 2\sigma_{12}\varepsilon_{12}^*\right]_{kl}\delta_{kl}. \tag{A3}$$

Lastly, the average strain energy for the entire sample is

$$< W(\omega) > = \sum_{k,l} < W(\omega)_{kl} > . \tag{A4}$$

It is important to mention that the attribute computed with equation (A1) does not depend on the amplitude of the applied strain in the relaxation tests (Rubino et al., 2016). Moreover, we have verified that $\sum_{k,l} < q_{kl}^{-1}(\omega) >$ for the horizontal and vertical relaxation tests equals $Q_{\mathrm{P}}^{-1}(\omega)$ computed using the effective $C_{ij}(\omega)$ coefficients given in equation (7) for horizontal and vertical P wave propagation, respectively.

Acknowledgments
The data derived by the numerical simulations and the underlying models can be obtained free of charge upon request from the lead author. This work was supported by a grant from the Swiss National Science Foundation and completed within SCCER-SoE with the support of CTI.

References

Bakulin, A., Grechka, Va., & Tsvankin, I. (2000). Estimation of fracture parameters from reflection seismic data-Part II: Fractured models with orthorhombic symmetry. *Geophysics*, *65*, 1803–1817.

Biot, M. A. (1941). General theory of three-dimensional consolidation. *Journal of Applied Physics*, *12*, 155–164.

Biot, M. A. (1962). Mechanics of deformation and acoustic propagation in porous media. *Journal of Applied Physics*, *33*, 1482–1498.

Brajanovski, M., Gurevich, B., & Schoenberg, M. (2005). A model for *P*-wave attenuation and dispersion in a porous medium permeated by aligned fractures. *Geophysical Journal International*, *163*, 372–384.

Brown, R. J., & Korringa, J. (1975). On the dependence of the elastic properties of a porous rock on the compressibility of the pore fluid. *Geophysics*, *40*, 608–616.

Carcione, J. M. (2007). *Wave fields in real media: Wave propagation in anisotropic, anelastic, porous and electromagnetic media*. Amsterdam, Netherlands: Elsevier.

Chapman, M. (2003). Frequency-dependent anisotropy due to meso-scale fractures in the presence of equant porosity. *Geophysical Prospecting*, *51*, 369–379.

Chapman, M. (2009). Modeling the effect of multiple sets of mesoscale fractures in porous rock on frequency-dependent anisotropy. *Geophysics*, *74*, 97–103.

Collet, O., & Gurevich, B. (2016). Frequency dependence of anisotropy in fluid saturated rocks-Part I: Aligned cracks case. *Geophysical Prospecting*, *64*, 1067–1084.

Ding, P., Di, B., Wang, D., Wei, J., & Li, X. (2017). Measurements of seismic anisotropy in synthetic rocks with controlled crack geometry and different crack densities. *Pure and Applied Geophysics*, *174*, 1907–1922.

Dubos-Sallée, N., & Rasolofosaon, P. N. (2011). Estimation of permeability anisotropy using seismic inversion for the CO2 geological storage site of Sleipner (North Sea). *Geophysics*, *76*, 63–69.

Dürrast, H., Rasolofosaon, P. N., & Siegesmund, S. (2002). *P*-wave velocity and permeability distribution of sandstones from a fractured tight gas reservoir. *Geophysics*, *67*, 241–253.
Gassmann, F. (1951). Elastic waves through a packing of spheres. *Geophysics*, *16*, 673–685.
Galvin, R. J., & Gurevich, B. (2015). Frequency-dependent anisotropy of porous rocks with aligned fractures. *Geophysical Prospecting*, *63*, 141–150.
Gelinsky, S., & Shapiro, S. A. (1997). Poroelastic Backus averaging for anisotropic layered fluid-and gas-saturated sediments. *Geophysics*, *62*, 1,867–1,878.
Guo, J., Rubino, J. G., Glubokovskikh, S., & Gurevich, B. (2016). Effects of fracture intersections on seismic dispersion: Theoretical predictions versus numerical simulations. *Geophysical Prospecting*, *65*, 1264–1276. https://doi.org/10.1111/1365-2478.12474
Laubach, S., Marrett, R., & Olson, J. (2000). New directions in fracture characterization. *The Leading Edge*, *19*, 704–711.
Liu, E., & Martinez, A. (2013). *Seismic fracture characterization: Concepts and practical applications*. Netherlands: EAGE.
Martin, N. W., & Brown, R. J. (1996). Compressional velocity, seismic attenuation and permeability relationships for sandstones from WOSPP (CREWES Research Report, Vol. 8).
Maultzsch, S., Chapman, M., Liu, E., & Li, X. Y. (2003). Modelling frequency-dependent seismic anisotropy in fluid-saturated rock with aligned fractures: Implication of fracture size estimation from anisotropic measurements. *Geophysical Prospecting*, *51*, 381–392.
Maultzsch, S., Chapman, M., Liu, E., & Li, X. Y. (2007). Modelling and analysis of attenuation anisotropy in multi-azimuth VSP data from the Clair field. *Geophysical Prospecting*, *55*, 627–642.
Mavko, G., Mukerji, T., & Dvorkin, J. (2009). *The rock physics handbook: Tools for seismic analysis of porous media*. Cambridge, UK: Cambridge University Press.
Milani, M., Monachesi, L., Sabbione, J. I., Rubino, J. G., & Holliger, K. (2016). A generalized effective anisotropic poroelastic model for periodically layered media accounting for both Biot's global and interlayer flows. *Geophysical Prospecting*, *64*, 1135–1148.
Müller, T. M., Gurevich, B., & Lebedev, M. (2010). Seismic wave attenuation and dispersion resulting from wave-induced flow in porous rocks: A review. *Geophysics*, *75*, 147–164.
Pride, S. R. (2005). Relationships between seismic and hydrological properties. In *Hydrogeophysics* (pp. 253–290). Netherlands: Springer.
Quintal, B., Jänicke, R., Rubino, J. G., Steeb, H., & Holliger, K. (2014). Sensitivity of *S*-wave attenuation to the connectivity of fractures in fluid-saturated rocks. *Geophysics*, *79*, WB15–WB24.
Rasolofosaon, P. N., & Zinszner, B. E. (2002). Comparison between permeability anisotropy and elasticity anisotropy of reservoir rocks. *Geophysics*, *67*, 230–240.
Rubino, J. G., & Holliger, K. (2013). Research note: Seismic attenuation due to wave-induced fluid flow at microscopic and mesoscopic scales. *Geophysical Prospecting*, *61*, 882–889.
Rubino, J. G., Caspari, E., Müller, T. M., & Holliger, K. (2017). Fracture connectivity can reduce the velocity anisotropy of seismic waves. *Geophysical Journal International*, *210*, 223–227.
Rubino, J. G., Guarracino, L., Müller, T. M., & Holliger, K. (2013). Do seismic waves sense fracture connectivity? *Geophysical Research Letters*, *40*, 692–696. https://doi.org/10.1002/grl.50127
Rubino, J. G., Müller, T. M., Guarracino, L., Milani, M., & Holliger, K. (2014). Seismoacoustic signatures of fracture connectivity. *Journal of Geophysical Research*, *119*, 2252–2271. https://doi.org/10.1002/2013JB010567
Rubino, J. G., Caspari, E., Müller, T. M., Milani, M., Barbosa, N. D., & Holliger, K. (2016). Numerical upscaling in 2-D heterogeneous poroelastic rocks: Anisotropic attenuation and dispersion of seismic waves. *Journal of Geophysical Research*, *121*, 6698–6721. https://doi.org/10.1002/2016JB013165
Sarout, J. (2012). Impact of pore space topology on permeability, cut-off frequencies and validity of wave propagation theories. *Geophysical Journal International*, *189*, 481–492.
Solazzi, S. G., Rubino, J. G., Müller, T. M., Milani, M., Guarracino, L., & Holliger, K. (2016). An energy-based approach to estimate seismic attenuation due to wave-induced fluid flow in heterogeneous poroelastic media. *Geophysical Journal International*, *207*, 823–832.
Schoenberg, M. A. (1980). Elastic wave behavior across linear slip interfaces. *Journal of the Acoustical Society of America*, *68*, 1516–1521.
Thomsen, L. (1986). Weak elastic anisotropy. *Geophysics*, *51*, 1954–1966.
Tillotson, P., Chapman, M., Sothcott, J., Best, A. I., & Li, X. Y. (2014). Pore fluid viscosity effects on *P*- and *S*-wave anisotropy in synthetic silica-cemented sandstone with aligned fractures. *Geophysical Prospecting*, *62*, 1238–1252.
Tsvankin, I. (1997). Anisotropic parameters and *P*-wave velocity for orthorhombic media. *Geophysics*, *62*, 1292–1309.
Vinci, C., Renner, J., & Steeb, H. (2014). On attenuation of seismic waves associated with flow in fractures. *Geophysical Research Letters*, *41*, 7515–7523.
Wang, Z. (2002). Seismic anisotropy in sedimentary rocks, part 2: Laboratory data. *Geophysics*, *67*, 1423–1440.
Zhang, Y., Sayers, C. M., & Adachi, J. I (2009). The use of effective medium theories for seismic wave propagation and fluid flow in fractured reservoirs under applied stress. *Geophysical Journal International*, *177*, 205–221.